The effect of magnesium on the structure of calcium aluminosilicate glasses

John Sedgwick and Russell J Hand

ISL, School of Chemical, Materials and Biological Engineering

University of Sheffield

Sir Robert Hadfield Building

Mappin Street

Sheffield, S1 3JD, UK

Abstract

Samples of cemented magnesium turnings and Magnox alloy, simulating wasteforms that require re-work, have been thermally treated to produce largely glassy calcium magnesium aluminosilicate products. X-ray diffraction shows the presence of a variety of $Mg_xAl_{2-x}O_4$ phases, åkermanite-gehlenite and merwinite phases, as well as diffuse scattering characteristic of glassy material. Structural investigations using Raman spectroscopy show that the products contain amorphous aluminosilicate networks, with changes in the Q_2 and Q_1 species in the network with increasing metal content. These investigations also suggest a high number of $[AlO_4]^-$ tetrahedra are present in the network.

Introduction

Magnox swarf arising from fuel reprocessing of the metallic nuclear fuel used in the UK's Magnox reactors is currently immobilised by cement encapsulation. However, corrosion of the swarf within cemented wastes can lead to wasteform expansion and cracking resulting in a need to re-work such wasteforms before any final disposal. As the compositions of the cements used are comparable to the glass forming region in the calcium aluminosilicate phase diagram re-work through vitrification may present an appropriate solution. This paper describes an initial investigation to assess the viability of this solution through the thermal treatment of inactive simulant cemented wasteforms.

Background

Historically spent nuclear fuel (SNF) from Magnox reactors in the UK was sent for reprocessing [1]. The Magnox fuel cladding consists of a magnesium alloy (AL80) containing 0·8% Al, 0·002-0·05% Be, 0·008% Ca and 0·006% Fe [2]. An early stage of reprocessing involved separating the Magnox cladding from the uranium fuel rods, after which it was stored in the Magnox Swarf Storage Silos (MSSS), and eventually encapsulated in a cementitious grout at the Magnox Encapsulation Plant (MEP) [3]. Typically, the grout used consisted of a 3:1 mixture of blast furnace slag (BFS) and Portland cement (PC) and after hydration the resulting cement thus mainly contains calcium silicate hydrates (CSHs), calcium aluminium silicate hydrates (CASHs) and calcium aluminium hydrates (CAHs). The cemented wasteforms are currently stored in above ground store pending a disposal route becoming available, which is likely to be in a geological disposal facility (GDF) designed to prevent the release of radioactive isotopes back to the biosphere for timescales of at least hundreds of thousands of years [4].

However, during storage, reaction of the Magnox alloy with the cement pore water results in $Mg(OH)_2$ as a corrosion product, alongside hydrogen:

$$Mg + 2H_2O \rightarrow Mg(OH)_2 + H_2 \quad (1)$$

In addition to this, the small amount of uranium metal present in each grouted waste package as a result of the shearing process, may also corrode [5], [6] again potentially resulting in hydrogen release:

$$U + 2H_2O \rightarrow UO_2 + 2H_2 \quad (2)$$

$$2U + 3H_2 \rightarrow 2UH_3 \quad (3)$$

As a result of these reactions, expansion of the wasteforms, and therefore cracking (and eventually failure) will occur over a period of several hundred years [1], [5], [6], [7], [8], [9]. Any wasteform disposed of in a GDF must be stable over geological timescales, meaning the stability of these grouted wasteforms is unacceptable [4], [10], [11]. One potential method for re-working such failed cementitious wasteforms is thermal treatment to produce a lower volume vitreous wasteform. Given the cement composition and the waste therein, minimal or no additions would likely be required to produce an alkaline earth aluminosilicate glass. Aluminosilicate glasses with a low alkali and moderate alkaline earth contents are widely used in the manufacture of display screen glass, glass fibres and halogen bulbs [12]. In addition calcium aluminosilicate glasses have received interest as potential wasteforms for chloride containing wastes [13], [14], [15].

As noted, glass production from such cemented wasteforms could potentially involve the addition of no further glass making materials and that option is explored here.

Materials and Methods

Two series of simulant wasteforms were produced, both with a 3:1 ground granulated blast furnace slag (GGBFS) to Portland cement (PC) grout with a 0·35 water to solid ratio. The GGBFS was sourced from Scunthorpe (LKAB Minerals) and the PC from Ribblesdale Cement Works (Heidelberg Materials). The first series of simulant wasteforms (MgT samples) contained up to 10 wt% magnesium turnings, and the second (MgA samples) contained up to 8 wt% Magnox Al-80 alloy. The ratios of grout to metal are shown in Table 1. The simulant cemented wasteforms were allowed to hydrate for 28 days before thermal treatment was undertaken.

Table 1: The ratios of grout to metal in each sample. MgT samples contain magnesium turnings and MgA samples contain Magnox alloy.

Sample Name	Grout (g)	Metal (g)	Total Weight (g)
MgT_0	50	0	50
MgT_1	49	1	50
MgT_2	48	2	50
MgT_3	47	3	50
MgT_4	46	4	50
MgT_5	45	5	50
MgA_0	50	0	50
MgA_1	49	1	50
MgA_2	48	2	50
MgA_3	47	3	50
MgA_4	46	4	50

After 28 d the hydrated simulant wasteform samples were placed in alumina crucibles (Almath) and heated to 1600 °C at 5 °C min^{-1} and held at temperature for 3 h in a Lenton 1700 °C chamber furnace. The MgT samples were poured and annealed at 700 °C for 1 h before being cooled to room temperature at 1 °C min^{-1}. One MgT sample (MgT_5) was too viscous to pour, and therefore was removed from the furnace and allowed to air cool. As the MgA samples were too viscous to pour at 1600°C, after 3 h they were removed from the melting furnace and allowed to air cool. Images of the two series of samples are shown in Figure 1 and Figure 2.

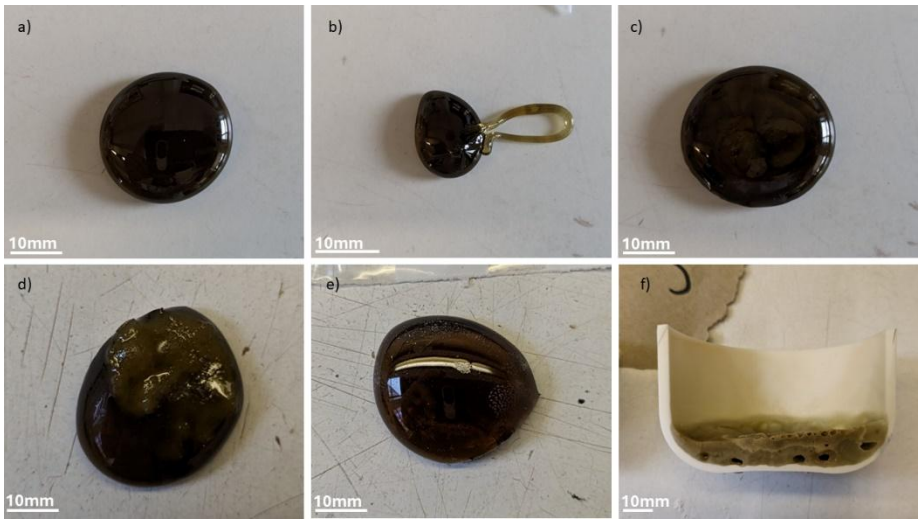

Figure 1: Images of the a) MgT_0, b) MgT_1, c) MgT_2, d) MgT_3, e) MgT_4, and e) MgT_5 samples after heating.

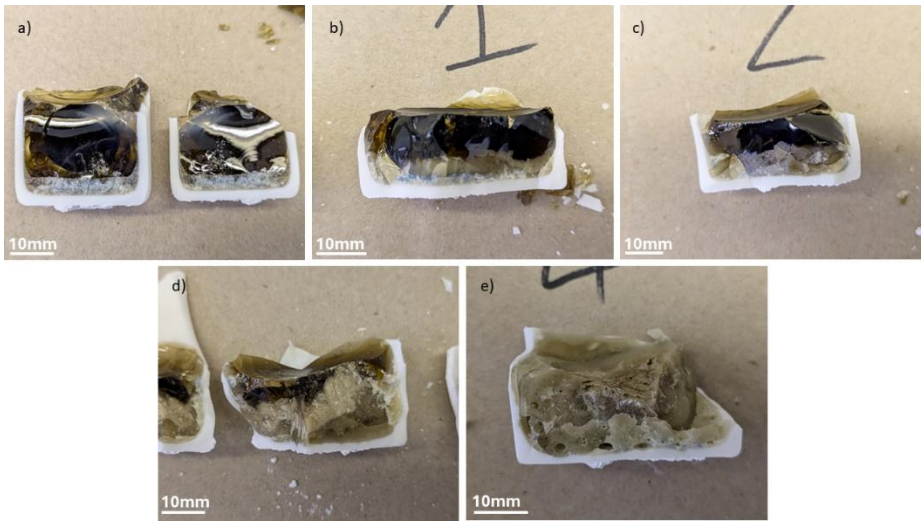

Figure 2: Images of the a) MgA_0, b) MgA_1, c) MgA_2, d) MgA_3, and e) MgA_4 samples after heating.

Samples in both series appeared glassy at low metal additions but contained a larger slag component and were more crystalline in appearance as the metal additions increased. Significant corrosion of the crucibles occurred for all samples.

Monolith and powder samples were prepared from both sets of glasses. Monoliths were taken from the samples using a Buehler IsoMet Low Speed Saw with a diamond wafering blade and mounted in epoxy resin. The mounted monoliths were successively ground and polished to a 1 µm finish using silicon carbide grinding discs, 6, 3 and 1 µm diamond pastes; isopropyl

alcohol (IPA) was used a coolant. Powder samples were prepared from the simulant wasteforms by crushing with an impact mortar and pestle followed by sieving to obtain the < 75 µm size fraction.

Structural analysis was conducted using powder X-ray diffraction (Panalytical XPert, using a Cu source with a CuK_β filter made of Ni from 10 to 70 °2θ) and Raman spectroscopy (Renishaw inVia Raman Microscope, using a 514 nm laser with a power of 20 mW). Chemical analysis was conducted using X-ray fluorescence (XRF) spectroscopy (Bruker Puma S2). XRF analysis was conducted on fused beads containing 1 g of sample and 10 g of a lithium tetraborate/lithium iodide flux produced by heating to 1065 °C in a Claisse LeNeo Fluxer. Microstructural analysis was undertaken using scanning electron microscopy (SEM) coupled with energy dispersive X-ray analysis (EDX) on an Inspect F50 microscope (using spot sizes of 3 and 3.5 at 20 kV). Crystallisation temperatures were identified using differential scanning calorimetry (DSC) on a TA Instruments SDT650 by heating to 1200 °C at 10 °C min^{-1} alongside an empty reference pan. Density was measured using helium pycnometry on a Micromeritics AccuPyc 1340 using a gas pressure of 13 psig (89631.8 Pa) for 5 cycles.

Results and Discussion

X-Ray Diffraction (XRD)

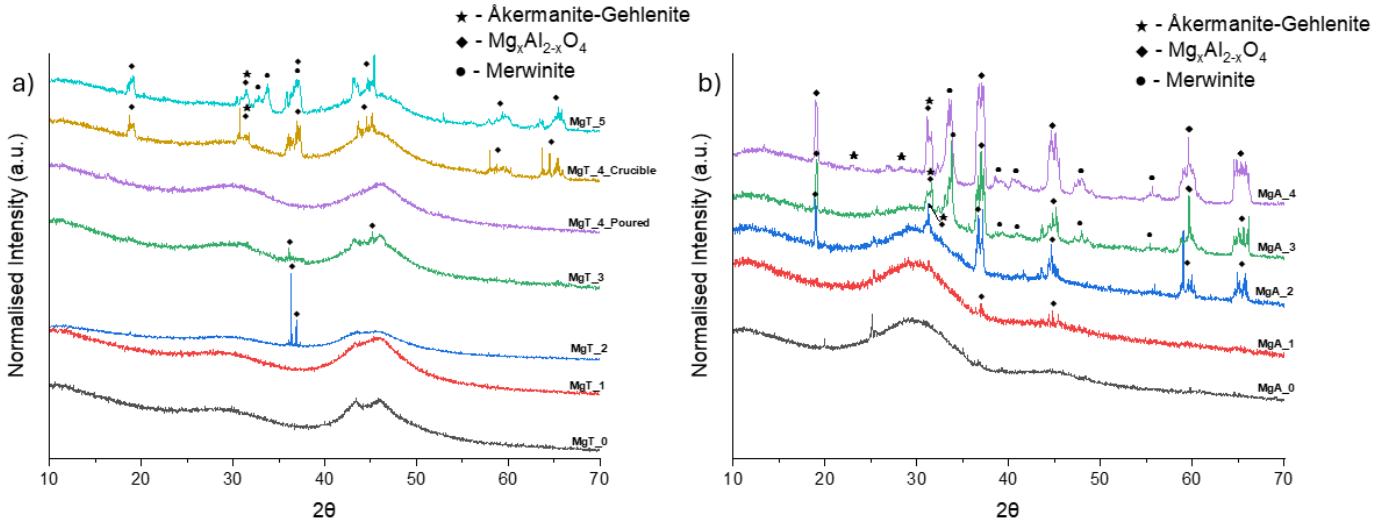

Figure 3: a) XRD patterns of the MgT samples and b) XRD patterns of the MgA samples. Diamonds indicate peaks assigned to $Mg_xAl_{2-x}O_4$, stars to peaks assigned to åkermanite-gehlenite, and circles to merwinite.

XRD patterns of the MgT samples show several broad and poorly defined peaks, alongside a diffuse scattering peak from 40 and 50 °2θ, and a less intense diffuse scattering region between 25 and 35 °2θ (see Figure 3a). The peaks can be assigned to $Mg_xAl_{2-x}O_4$, calcium magnesium aluminosilicate (åkermanite-gehlenite), and calcium magnesium silicate (merwinite) phases. The XRD patterns of the MgA samples show several peaks in the same locations as the MgT samples above (see Figure 3b) which are again assigned to $Mg_xAl_{2-x}O_4$, åkermanite-gehlenite and merwinite phases. However, in the MgA case the peaks are narrower and more well defined suggesting a higher degree of crystallinity. Again, there are diffuse scattering features between 25 and 35 °2θ, as well as between 40 and 50 °2θ, in this case the latter being less intense. No peaks that would be indicative of the presence of Mg metal or any Mg-Al alloys were present in

the MgT or MgA XRD patterns, indicating that most or all of the added metallic component had been oxidised.

X-Ray Fluorescence (XRF)

Semi-quantitative XRF was undertaken in order to calculate an approximate oxide composition of all samples produced, as well as the compositions of the grout, OPC and BFS prior to heating. The approximate compositions of the precursor materials are shown in Table 2, and those of the samples after heating in Table 3. Comparing the two rightmost columns of Table 2 indicates that the measured composition of the prepared grout is consistent with that expected based on the measured compositions of the OPC and BFS. The molar ratios of CaO: Al_2O_3: SiO_2 for the grout are 54·69: 7·79: 37·52. This is very close to the belite – rankinite – gehlenite boundary of the ternary CaO-Al_2O_3-SiO_2 phase diagram and lies within the glass forming region (shown in Figure 4).

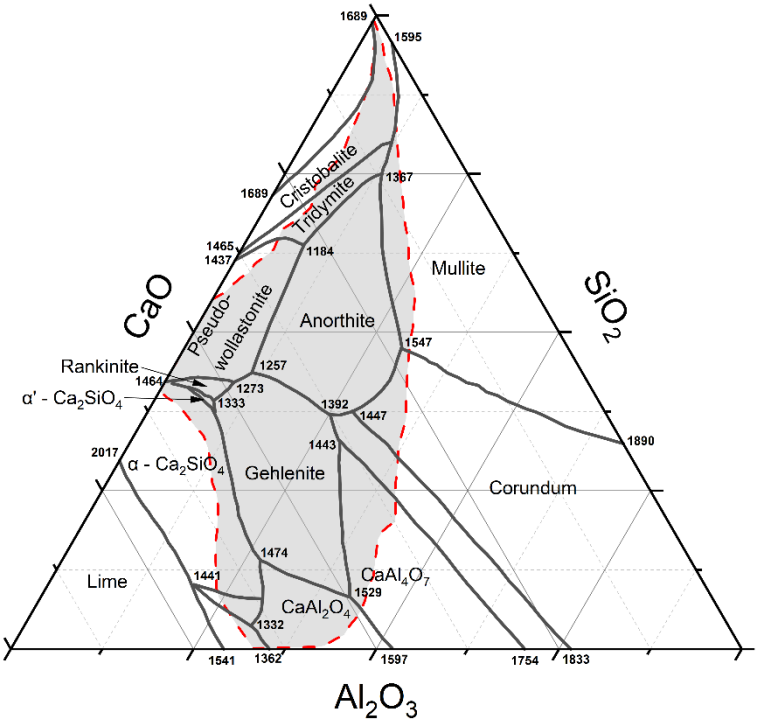

Figure 4: The ternary CaO-Al2O3-SiO2 phase diagram in mol%, with the glass forming region marked with a shaded area. This diagram is adapted from the diagram found in wt% on the FactSage software, with the glass forming region taken from Richet et al [16], [17].

Table 2: Oxide compositions assessed by semi-quantitative XRF of the OPC, and BFS used to produce the grout, and of the grout itself prior to heating. All values are in mol%.

Oxide	OPC	BFS	Grout	Calculated 3:1 BFS:OPC
MgO	2·78	13·72	10·31	10·99
Al_2O_3	2·77	8·01	6·76	6·70
SiO_2	21·44	36·55	32·55	32·77
SO_3	2·57	0·30	1·09	0·87
K_2O	0·53	0·55	0·57	0·55
CaO	68·55	39·76	47·45	46·96
Sc_2O_3	0·05	0·00	0·00	0·01
TiO_2	0·09	0·36	0·33	0·29
Cr_2O_3	0·01	0·00	0·00	0·00
MnO	0·04	0·37	0·29	0·29
Fe_2O_3	1·07	0·33	0·58	0·52
NiO	0·00	0·00	0·01	0·00
ZnO	0·01	0·00	0·00	0·00
SrO	0·07	0·05	0·05	0·06
Total	99·98	100·00	99·99	100·01

Table 3: Oxide compositions assessed by semi-quantitative XRF of all samples produced after heating. All values are in mol%.

Oxide	MgA_0	MgA_1	MgA_2	MgA_3	MgA_4	MgT_0	MgT_1	MgT_2	MgT_3	MgT_4	MgT_5
Na_2O	0·00	0·00	0·00	0·00	0·00	0·28	0·26	0·22	0·25	0·29	0·31
MgO	8·94	13·54	18·92	23·13	29·58	9·89	13·26	17·27	18·91	23·00	32·85
Al_2O_3	26·04	22·54	23·55	23·71	27·28	29·31	25·41	23·47	20·58	17·23	24·14
SiO_2	27·32	27·26	23·75	21·71	17·40	25·33	26·62	25·68	23·45	23·86	17·99
SO_3	0·00	0·00	0·00	0·00	0·00	0·00	0·00	0·00	0·00	0·00	0·00
K_2O	0·49	0·47	0·44	0·42	0·39	0·27	0·25	0·24	0·25	0·20	0·30
CaO	36·28	35·25	32·49	30·24	24·62	33·89	33·15	32·15	35·52	34·27	23·60
TiO_2	0·24	0·25	0·21	0·19	0·15	0·29	0·31	0·30	0·31	0·30	0·18
MnO	0·22	0·21	0·20	0·19	0·17	0·22	0·21	0·20	0·23	0·24	0·20
Fe_2O_3	0·44	0·44	0·40	0·39	0·39	0·38	0·38	0·33	0·38	0·45	0·34
SrO	0·05	0·03	0·03	0·03	0·03	0·03	0·04	0·03	0·04	0·06	0·02
Rh_2O_3	0·00	0·00	0·00	0·00	0·00	0·00	0·00	0·00	0·00	0·00	0·00
BaO	0·00	0·00	0·00	0·00	0·00	0·03	0·03	0·02	0·06	0·07	0·03

The XRF data for both the MgT and MgA sample series show an increase in MgO content which is in line with the amount of metal added to each sample. A much higher alumina content is observed in all samples than in the original grout, which is due to the corrosion of the crucibles. For the samples with no metal additions namely MgA_0 and MgT_0 the CaO: Al_2O_3: SiO_2 molar ratios are 40·47: 29·05: 30·48 and 38·28: 33·11: 28·61 respectively – the higher alumina value in the latter case will reflect the crucible cooling of this sample. The former is on the gehlenite-grossite phase boundary whereas the latter is within the grossite region of the CaO-Al_2O_3-SiO_2 phase diagram; despite the significantly high alumina content both points still lie within the glass forming region.

Scanning Electron Microscopy (SEM)

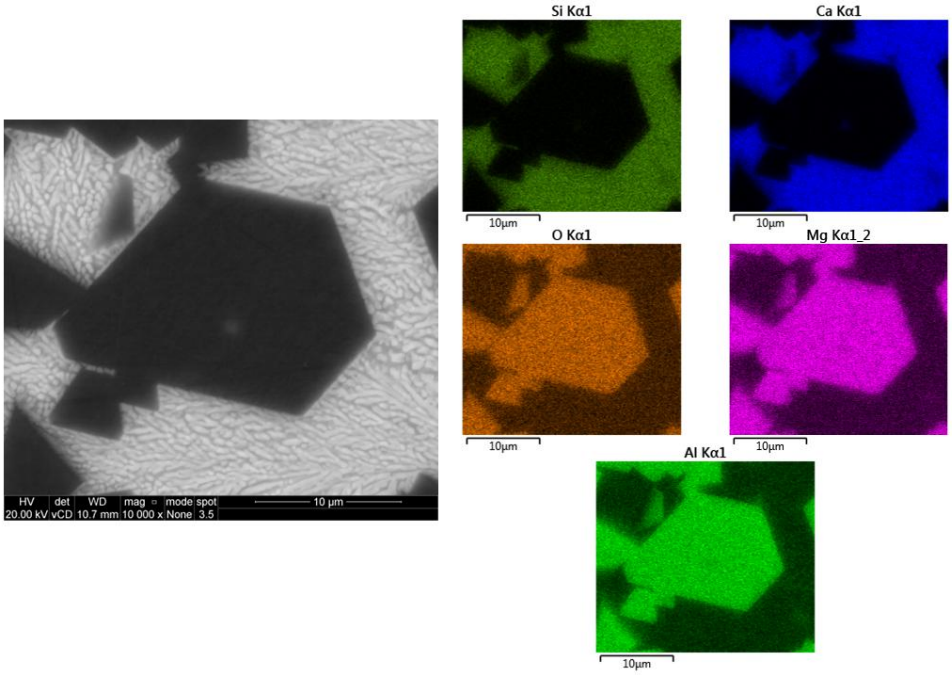

Figure 5: BSE image of the MgT_5 sample with associated EDX maps

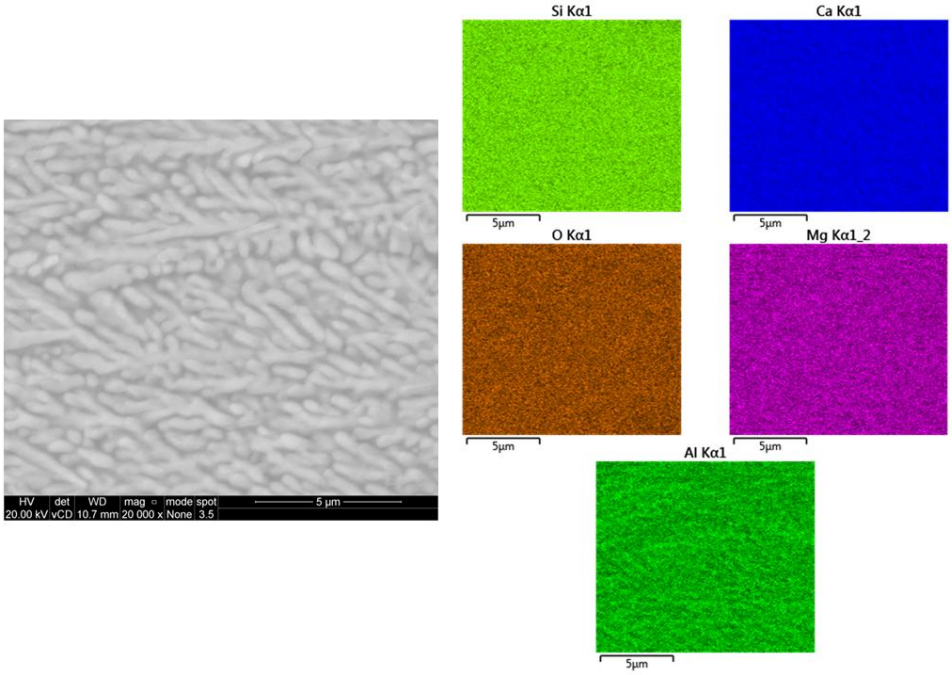

Figure 6: BSE image of the MgT_5 sample at 20 000X magnification with associated EDX maps

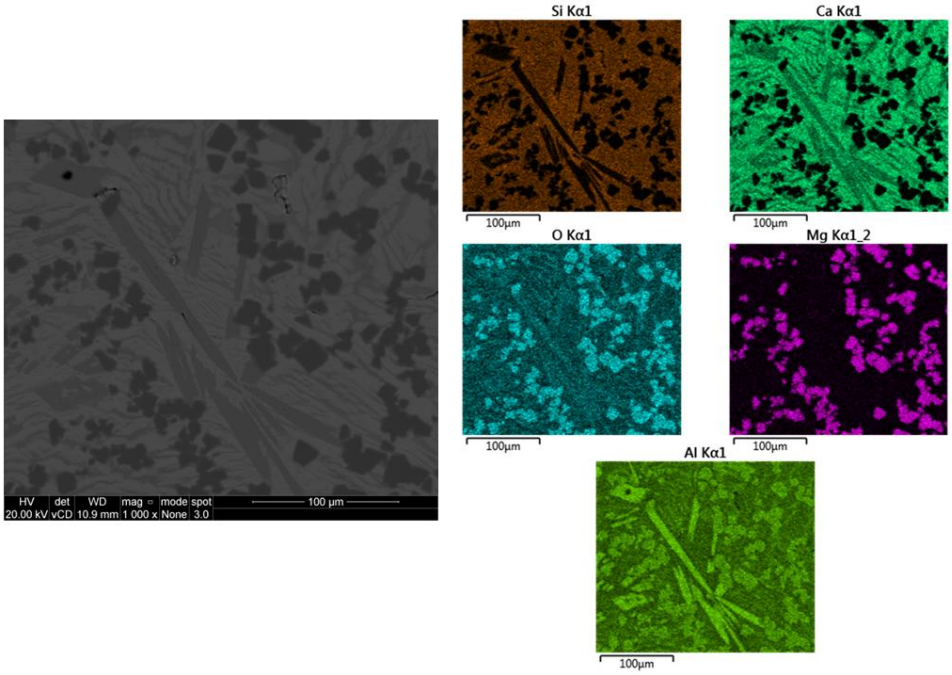

Figure 7: BSE image of the MgA_4 sample with the associated EDX maps

SEM of the MgT_5 sample (Figure 5) shows well defined crystals appearing dark in BSE image that can be seen throughout the sample. These regions have high concentrations of Mg, Al and O, and are therefore be assumed to be the $Mg_xAl_{2-x}O_4$ phase identified by XRD. Similar crystals were seen in MgT_2 to MgT_4. In this sample, evidence of phase separation is also observed in the lighter regions of the BSE image. This region is Ca, Al, and Si rich however no compositional differences can be seen in the elemental maps although some Z-contrast is visible in the BEI image. Imaging at 20 000X magnification away from the $Mg_xAl_{2-x}O_4$ phase shows slight variation in the Al content in this region, with Mg also present (shown in Figure 6).

Figure 7 shows a region of the MgA_4 sample adjacent to the crucible edge. Again, three separate phases can be identified in the BSE image, although their detailed morphology differs from that seen in the MgT_5 sample. Similarly to the MgT_5 sample, sharp crystalline regions containing Mg, Al, and O are present indicating an $Mg_xAl_{2-x}O_4$ phase. In addition to this, a series of needle like regions are present. The EDX maps of the needle like regions show a high concentration of Al and O with an intermediate level of Ca. Material rich in Si and Ca is also present.

Differential Scanning Calorimetry (DSC)

Table 4: Crystallisation temperatures as determined by DSC for each sample.

Sample	Crystallisation T (°C)	Sample	Crystallisation T (°C)
MgT_0	1008	MgA_0	974
MgT_1	986	MgA_1	957
MgT_2	970	MgA_2	951
MgT_3	957	MgA_3	951
MgT_4	950	MgA_4	984
MgT_5	986		

DSC was used to investigate the crystallisation of the heat-treated materials. The position of some peaks of interest are listed in Table 4. The main observable feature is an exothermic peak across all samples between 950 °C and 1010 °C. Following thermal treatment of samples at 950°C, this peak was determined to be likely due to the crystallisation of the calcium magnesium aluminosilicate (åkermanite-gehlenite) phase previously observed in XRD.

Density Analysis

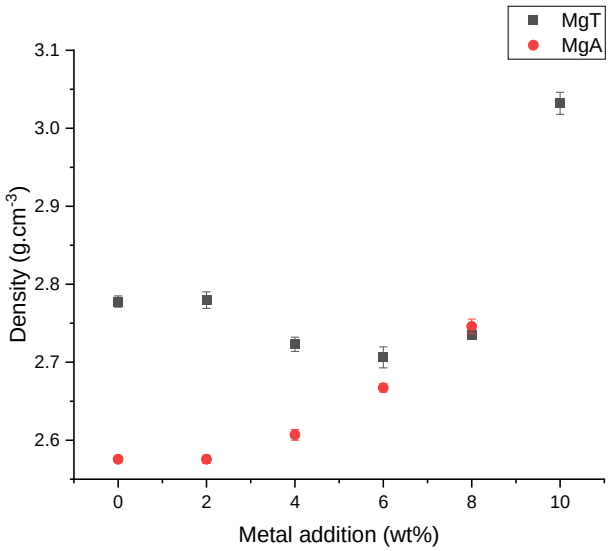

Figure 8: Densities of the heat-treated samples.

The density of the MgT samples (shown in Figure 8) remains relatively consistent up until 10 wt% magnesium turnings (MgT_5), where an ~ 10 % increase in density is observed. The higher density of the MgT_5 sample is likely because of its high degree of crystallinity. The slight decrease in the densities of the MgT_3 and MgT_4 samples may be related to their lower Al_2O_3

contents compared to the other samples (see Table 3). The density of the MgA samples increases with increasing Magnox alloy content. This is likely due to the increasing crystallinity of the samples, with the $Mg_xAl_{2-x}O_4$ phases having a theoretical density of over 3·5 g cm^{-3} [18].

Raman Spectroscopy

Raman spectroscopy was used to investigate the structure of the heat-treated materials. A useable Raman spectrum could not be obtained from the crystalline regions due to fluorescence; hence no spectra were obtained for the MgT_5 and MgA_4 samples. The Raman spectra of the MgT samples is shown in Figure 9, and the spectra for the MgA samples are shown in Figure 10. Background subtraction was undertaken on the spectra using a third order polynomial using the rampy python library [19].

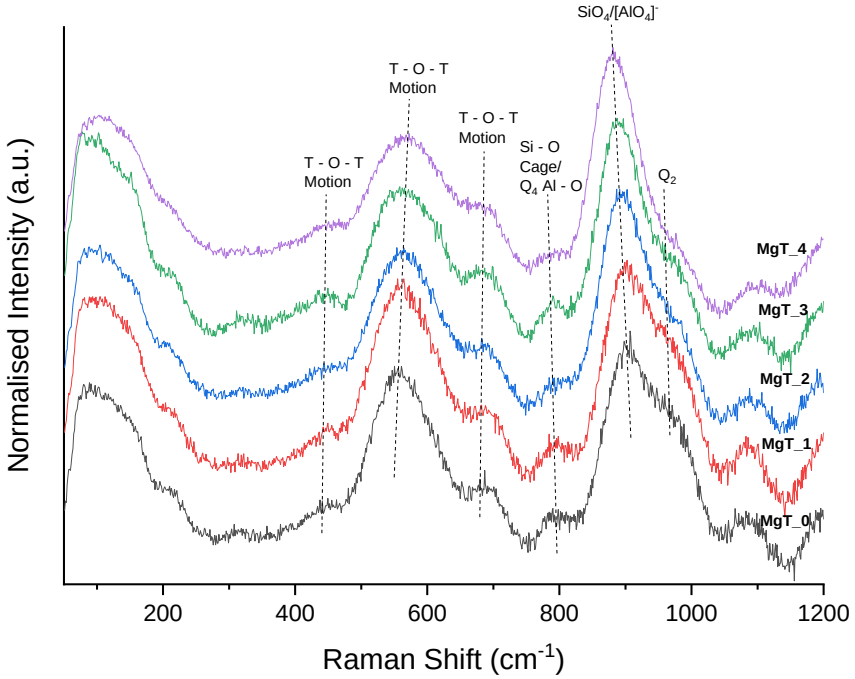

Figure 9: Raman spectra of the MgT samples.

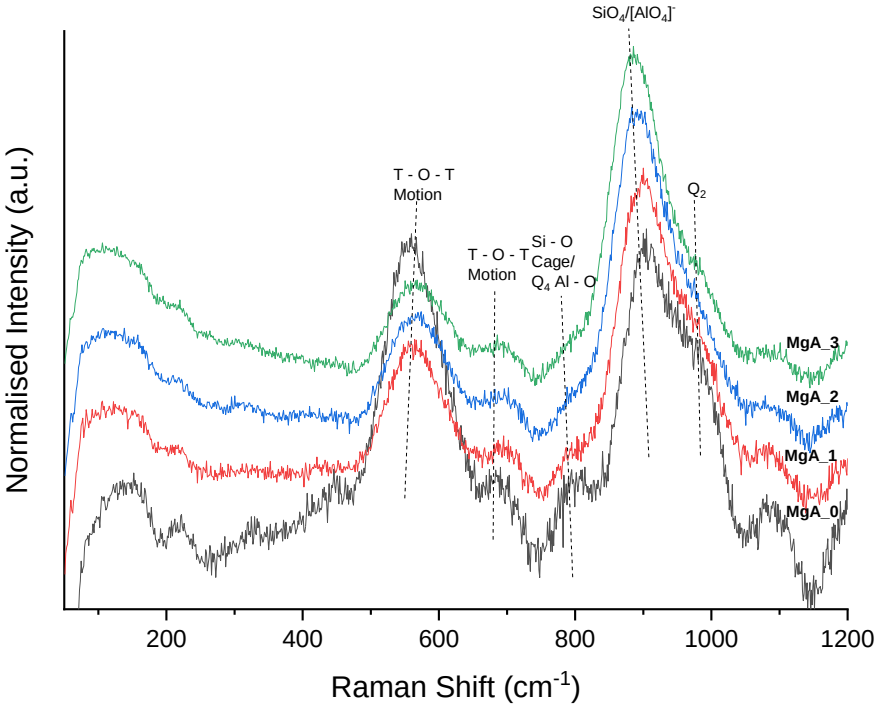

Figure 10: Raman spectra of the MgA samples.

There are three main areas of interest in the Raman spectra: a low frequency region from 200 cm^{-1} to 700 cm^{-1}, an intermediate frequency region from 700 cm^{-1} to 900 cm^{-1}, and a high frequency region from 900 cm^{-1} to 1300 cm^{-1}.

Low Frequency Region

The dominant band in this region for both samples is centred around 560 cm^{-1} and shifts slightly to higher wavenumbers (570 cm^{-1}) with increasing MgO content. This band can be attributed to the bending motion of T – O – T bonds within the glass network [20], [21], [22]. The intensity of this band suggests that a significant quantity of Al^{3+} ions have been substituted into the network to form $[AlO_4]^-$ tetrahedra in the MgT_0 sample [20], [21], [22]. Reduction of intensity in this band occurs gradually with increasing Mg content for the MgT samples and may be a sign of depolymerisation of the network. However, unlike the MgT samples, there is a significant change in relative intensity between the MgA_0 sample and those containing Magnox metal, especially in going from the MgA_0 to MgA_1 sample. To either side of this main band are two shoulders, one at approximately 450 cm^{-1} (only present in the MgT samples) and one at approximately 680 cm^{-1}. Similarly to the dominant band, the shoulder at 450 cm^{-1} can be attributed to the bending motion of T – O – T bonds within the glass network, and likely arises as a result of SiO_4 tetrahedra [20], [21], [22]. It may also be attributed to the presence of tetrahedra in five, six and seven membered rings within the glass network [23], [24]. The shoulder at 680 cm^{-1} may be attributed to T – O – T linkages within the silica network [25].

Intermediate Frequency Region

In this region, a small band is visible at 800 cm^{-1} in both samples which may be attributed to movement of Si within its oxygen cage [20], [21], [26], [27], or it may also be attributed to the motion of Al – O bonds in $[AlO_4]^-$ tetrahedra in Q_4 units [28]. This band remains relatively constant in the MgT samples. However, in the MgA samples, this band significantly reduces in intensity. This, in tandem with the previous XRF data, would suggest that the composition of the network is becoming less silica rich, as this feature is seen most predominantly above 50 mol% SiO_2 [20], [21], [26].

High Frequency Region

The first peak of interest in this region is centred at 900 cm^{-1} for the initial MgT sample and shifts to 880 cm^{-1} for the sample with the most MgO. Similarly, the initial MgA sample has a main peak centred at 905 cm^{-1} which shifts to 885 cm^{-1} for the MgA_4 sample. These peaks are likely comprised of contributions from several bands, namely the stretching vibrations of Q_2 and Q_3 Al – O bonds within $[AlO_4]^-$ tetrahedra and the stretching vibrations of Q_1 units within the silica network [20], [22], [29], [30]. The shift of these main peaks towards lower wavenumbers may be representative of a depolymerisation of the silica network, or the change in environment caused by the substitution of Mg^{2+} ions for Ca^{2+} ions around NBOs. This shift may also be because of Mg^{2+} ions substituting into the network to form $[MgO_4]^{2-}$ tetrahedra. There is a large shoulder on this main peak of both sample series at approximately 960 cm^{-1} that reduces in intensity with increasing MgO content. This band can be attributed to the stretching of Q_2 units in the silica network [23], [29], [31]. The reduction of intensity of this band suggests the number of Q_2 units in the network is decreasing and may support the idea that the network is being depolymerised.

Conclusions

The aim of this work was to assess the viability of vitrification and thermal treatment as a method of consolidating failed and failing grouted wasteforms. This has been achieved through heating at high temperature, with a multi-phase glass ceramic being produced. This product appeared to contain no metal, suggesting the entirety of the original metallic waste had been oxidised and fully incorporated into either the amorphous matrix or the crystalline phases. Due to corrosion of the alumina crucibles used all samples contained a significantly larger amount of alumina than would have been expected based solely on the grout composition, but (when considered purely on the ratio of CaO, Al_2O_3, and SiO_2) the composition remained in the glass forming region of the CAS ternary phase diagram. However, the increased alumina content likely promoted the formation of the $MgAl_2O_4$ phase seen with increasing Mg content in both series of samples. Analysis of the densities of the samples shows an increase in line with the increasing crystallinity of the samples. Raman spectroscopy indicated that considerable numbers of $[AlO_4]^-$ tetrahedra had been formed with charge balance presumably provided by alkaline earths rather than alkalis given the composition. The highly connected nature of the glasses (and hence melts) will be responsible for the elevated processing temperatures required to produce these materials.

Overall, the trials can be considered successful, as a consolidated wasteform was produced. However, for this approach to be viable in a nuclear context it will require further developmental work, initially focussing on reducing the processing temperatures. This is required to minimise volatilisation of common problematic isotopes such as ^{137}Cs during re-work of failed and failing wasteforms. It may also be pertinent to assess the chemical durability of any final products using a standardized methodology such as the product consistency test (PCT).

References

[1] G. A. Fairhall and J. D. Palmer, 'The encapsulation of Magnox Swarf in cement in the United Kingdom', *Cem. Concr. Res.*, vol. 22, no. 2–3, pp. 293–298, Mar. 1992, doi: 10.1016/0008-8846(92)90068-7.

[2] P. D. Wilson, *Nuclear Fuel Cycle, The: From Ore to Waste*. Oxford, UNITED KINGDOM: Oxford University Press, 1996. Accessed: Sep. 16, 2024. [Online]. Available: http://ebookcentral.proquest.com/lib/sheffield/detail.action?docID=4962953

[3] M. Moore, 'Encapsulation - dealing with swarf', *Nucl. Eng.*, vol. 31, no. 5, pp. 149–150, 1990.

[4] International Atomic Energy Agency, 'Scientific and Technical Basis for the Geological Disposal of Radioactive Wastes', International Atomic Energy Agency, Text, 2003. Accessed: Sep. 04, 2024. [Online]. Available: https://www.iaea.org/publications/6568/scientific-and-technical-basis-for-the-geological-disposal-of-radioactive-wastes

[5] C. A. Stitt *et al.*, 'An Investigation on the Persistence of Uranium Hydride during Storage of Simulant Nuclear Waste Packages', *PLOS ONE*, vol. 10, no. 7, p. e0132284, Jul. 2015, doi: 10.1371/JOURNAL.PONE.0132284.

[6] M. Sutton, P. Warwick, and A. Hall, 'Uranium(VI) interactions with OPC/PFA grout', *J. Environ. Monit.*, vol. 5, no. 6, pp. 922–928, Nov. 2003, doi: 10.1039/B308554F.

[7] J. Cronin and N. Collier, ‘Corrosion and expansion of grouted Magnox’, *Mineral. Mag.*, vol. 76, no. 8, pp. 2901–2909, Dec. 2012, doi: 10.1180/MINMAG.2012.076.8.05.

[8] C. Paraskevoulakos, K. R. Hallam, and T. B. Scott, ‘Grout durability within miniaturised Intermediate Level Waste drums at early stages of interior volume expansion induced by encapsulated metallic corrosion’, *J. Nucl. Mater.*, vol. 510, pp. 348–359, Nov. 2018, doi: 10.1016/J.JNUCMAT.2018.08.028.

[9] P. Potts, Alex Darren, ‘Reference package and factors affecting package evolution and degradation’, Nantional Nuclear Laboratory, Technical Memorandum D7.2.2, Aug. 2021. [Online]. Available: https://predis-h2020.eu/wp-content/uploads/2021/09/PREDIS_MS50-T7.2.2.-Reference-package-and-factors-affecting-package-evolution-and-degradation_Final-31.8.2021.pdf

[10] A. I. Marsh, L. G. Williams, and J. A. Lawrence, ‘The important role and performance of engineered barriers in a UK geological disposal facility for higher activity radioactive waste’, *Prog. Nucl. Energy*, vol. 137, p. 103736, Jul. 2021, doi: 10.1016/j.pnucene.2021.103736.

[11] C. L. Thorpe *et al.*, ‘Forty years of durability assessment of nuclear waste glass by standard methods’, *Npj Mater. Degrad.*, vol. 5, no. 1, p. 61, Dec. 2021, doi: 10.1038/s41529-021-00210-4.

[12] A. K. Varshneya, *Fundamentals of Inorganic Glasses*. London: Academic Press Limited, 1994.

[13] S. Siwadamrongpong, M. Koide, and K. Matusita, ‘Prediction of chloride solubility in CaO–Al2O3–SiO2 glass systems’, *J. Non-Cryst. Solids*, vol. 347, no. 1–3, pp. 114–120, Nov. 2004, doi: 10.1016/j.jnoncrysol.2004.07.063.

[14] J. M. Schofield, ‘Vitrification of a Chloride Containing Actinide Waste Surrogate’, University of Sheffield, 2011.

[15] S. Tan and R. J. Hand, ‘Incorporation and phase separation of Cl in alkaline earth aluminosilicate glasses’, *J. Nucl. Mater.*, vol. 507, pp. 135–144, Aug. 2018, doi: 10.1016/J.JNUCMAT.2018.04.044.

[16] C. W. Bale *et al.*, ‘FactSage thermochemical software and databases — recent developments’, *Calphad*, vol. 33, no. 2, pp. 295–311, Jun. 2009, doi: 10.1016/J.CALPHAD.2008.09.009.

[17] P. Richet, M. Roskosz, and J. Roux, ‘Glass formation in silicates: Insights from composition’, *Chem. Geol.*, vol. 225, no. 3–4, pp. 388–401, Jan. 2006, doi: 10.1016/J.CHEMGEO.2005.08.030.

[18] C. Gajdowski *et al.*, ‘Mechanical and optical properties of MgAl2O4 ceramics and ballistic efficiency of spinel based armour’, *Ceram. Int.*, vol. 48, no. 13, pp. 18199–18211, Jul. 2022, doi: 10.1016/j.ceramint.2022.03.079.

[19] C. L. Losq, *Rampy: a Python library for processing spectroscopic (IR, Raman, XAS...) data*. (Apr. 04, 2024). Zenodo. doi: 10.5281/zenodo.5557068.

[20] D. R. Neuville, L. Cormier, and D. Massiot, ‘Al coordination and speciation in calcium aluminosilicate glasses: Effects of composition determined by 27Al MQ-MAS NMR and Raman

spectroscopy', *Chem. Geol.*, vol. 229, no. 1–3, pp. 173–185, May 2006, doi: 10.1016/J.CHEMGEO.2006.01.019.

[21] D. R. Neuville, L. Cormier, and D. Massiot, 'Al environment in tectosilicate and peraluminous glasses: A 27Al MQ-MAS NMR, Raman, and XANES investigation', *Geochim. Cosmochim. Acta*, vol. 68, no. 24, pp. 5071–5079, Dec. 2004, doi: 10.1016/j.gca.2004.05.048.

[22] P. McMillan and B. Piriou, 'Raman spectroscopy of calcium aluminate glasses and crystals', *J. Non-Cryst. Solids*, vol. 55, no. 2, pp. 221–242, May 1983, doi: 10.1016/0022-3093(83)90672-5.

[23] C. Le Losq, D. R. Neuville, P. Florian, G. S. Henderson, and D. Massiot, 'The role of Al3+ on rheology and structural changes in sodium silicate and aluminosilicate glasses and melts', *Geochim. Cosmochim. Acta*, vol. 126, pp. 495–517, Feb. 2014, doi: 10.1016/J.GCA.2013.11.010.

[24] C. Le Losq and D. R. Neuville, 'Effect of the Na/K mixing on the structure and the rheology of tectosilicate silica-rich melts', *Chem. Geol.*, vol. 346, pp. 57–71, May 2013, doi: 10.1016/j.chemgeo.2012.09.009.

[25] A. Katerinopoulou, M. Musso, and G. Amthauer, 'A Raman spectroscopic study of the phase transition in omphacite', *Vib. Spectrosc.*, vol. 48, no. 2, pp. 163–167, Nov. 2008, doi: 10.1016/j.vibspec.2007.12.015.

[26] P. F. McMillan, B. T. Poe, P. H. Gillet, and B. Reynard, 'A study of SiO2 glass and supercooled liquid to 1950 K via high-temperature Raman spectroscopy', *Geochim. Cosmochim. Acta*, vol. 58, no. 17, pp. 3653–3664, Sep. 1994, doi: 10.1016/0016-7037(94)90156-2.

[27] P. McMillan, B. Piriou, and A. Navrotsky, 'A Raman spectroscopic study of glasses along the joins silica-calcium aluminate, silica-sodium aluminate, and silica-potassium aluminate', *Geochim. Cosmochim. Acta*, vol. 46, no. 11, pp. 2021–2037, Nov. 1982, doi: 10.1016/0016-7037(82)90182-X.

[28] C. Huang and E. C. Behrman, 'Structure and properties of calcium aluminosilicate glasses', *J. Non-Cryst. Solids*, vol. 128, no. 3, pp. 310–321, May 1991, doi: 10.1016/0022-3093(91)90468-L.

[29] P. McMillan, 'Structural Studies of Silicate Glasses and Melts-Applications and Limitations of Raman Spectroscopy', *Am. Mineral. - AMER Miner.*, vol. 69, pp. 622–644, Jul. 1984.

[30] X. Tang *et al.*, 'Quantitative studies on the microstructure of ternary CaO–Al2O3–SiO2 glasses by Raman spectroscopy, 27Al MAS NMR and quantum chemistry ab initio calculation', *Ceram. Int.*, vol. 49, no. 22, pp. 34397–34408, Nov. 2023, doi: 10.1016/J.CERAMINT.2023.07.150.

[31] J. Tan, S. Zhao, W. Wang, G. Davies, and X. Mo, 'The effect of cooling rate on the structure of sodium silicate glass', *Mater. Sci. Eng. B*, vol. 106, no. 3, pp. 295–299, Feb. 2004, doi: 10.1016/j.mseb.2003.09.045.